nature physics

Article

https://doi.org/10.1038/s41567-022-01809-3

Evidence for suprathermal ion distribution in burning plasmas

Received: 31 January 2022

Accepted: 29 September 2022

Published online: 14 November 2022

Check for updates

E. P. Hartouni[1] ✉, A. S. Moore[1] ✉, A. J. Crilly[2] ✉, B. D. Appelbe[2], P. A. Amendt[1], K. L. Baker[1], D. T. Casey[1], D. S. Clark[1], T. Döppner[1], M. J. Eckart[1], J. E. Field[1], M. Gatu-Johnson[3], G. P. Grim[1], R. Hatarik[1], J. Jeet[1], S. M. Kerr[1], J. Kilkenny[4], A. L. Kritcher[1], K. D. Meaney[5], J. L. Milovich[1], D. H. Munro[1], R. C. Nora[1], A. E. Pak[1], J. E. Ralph[1], H. F. Robey[1], J. S. Ross[1], D. J. Schlossberg[1], S. M. Sepke[1], B. K. Spears[1], C. V. Young[1] & A. B. Zylstra[1]

At the National Ignition Facility, inertial confinement fusion experiments aim to burn and ignite a hydrogen plasma to generate a net source of energy through the fusion of deuterium and tritium ions. The energy deposited by α-particles released from the deuterium–tritium fusion reaction plays the central role in heating the fuel to achieve a sustained thermonuclear burn. In the hydrodynamic picture, α-heating increases the temperature of the plasma, leading to increased reactivity because the mean ion kinetic energy increases. Therefore, the ion temperature is related to the mean ion kinetic energy. Here we use the moments of the neutron spectrum to study the relationship between the ion temperature (measured by the variance in the neutron kinetic energy spectrum) and the ion mean kinetic energy (measured by the shift in the mean neutron energy). We observe a departure from the relationship expected for plasmas where the ion relative kinetic energy distribution is Maxwell–Boltzmann, when the plasma begins to burn. Understanding the cause of this departure from hydrodynamic behaviour could be important for achieving robust and reproducible ignition.

The laser indirect-drive inertial confinement fusion (LID-ICF) at the National Ignition Facility (NIF) uses a hohlraum to convert laser energy into X-rays that symmetrically implode a capsule loaded with deuterium–tritium (DT) fuel (Fig. 1a). Lasers enter the top and bottom of the Au or depleted-uranium hohlraum, heating it with approximately 2 MJ of laser energy and irradiating the capsule with approximately 200 kJ of X-rays from a 300 eV X-ray spectrum. This ablates the layer of material (for the capsules considered here, high-density carbon (HDC)) surrounding a DT ice layer accelerating the capsule shell up to about 380–390 km s^{-1}. This results in the compression of DT ice and the generation of a hot-spot plasma through pressure–volume work on the DT gas that fills the centre of the capsule[1]. Fusion reactions (D + T → α + n + 17.59 MeV) begin to occur in the hot-spot plasma as this is compressed and heated to ~4–5 keV. Once a sufficient flux of α-particles (^{4}He) is generated by the fusion reactions, the surrounding dense DT fuel is heated by the energy loss of the α-particles leaving the central core, leading to 'run-away' heating that ignites the fuel (Fig. 1b, schematic). The details of the α-particle energy deposition as it is transported through the plasma and into the fuel are important for achieving the burning-plasma regime, the condition in which this α-energy exceeds the energy of the hot spot[2]. The dominance of the α-heating process, leading to the generation of a burning plasma, has been recently reported[3,4] for two-shot campaigns at the NIF.

Since the α-particles generated in the fusion reaction are stopped by the dense fuel surrounding the hot spot and do not escape the implosion, key physics performance parameters are determined by measuring the spectrum of the escaping neutrons. At the NIF, these

[1]Lawrence Livermore National Laboratory, Livermore, CA, USA. [2]Centre for Inertial Fusion Studies, The Blackett Laboratory, Imperial College, London, UK. [3]Massachusetts Institute of Technology, Plasma Science and Fusion Center, Cambridge, MA, USA. [4]General Atomics, San Diego, CA, USA. [5]Los Alamos National Laboratory, Los Alamos, NM, USA. ✉e-mail: ed_hartouni@comcast.net; moore212@llnl.gov; a.crilly16@imperial.ac.uk

https://doi.org/10.1038/s41567-022-01809-3

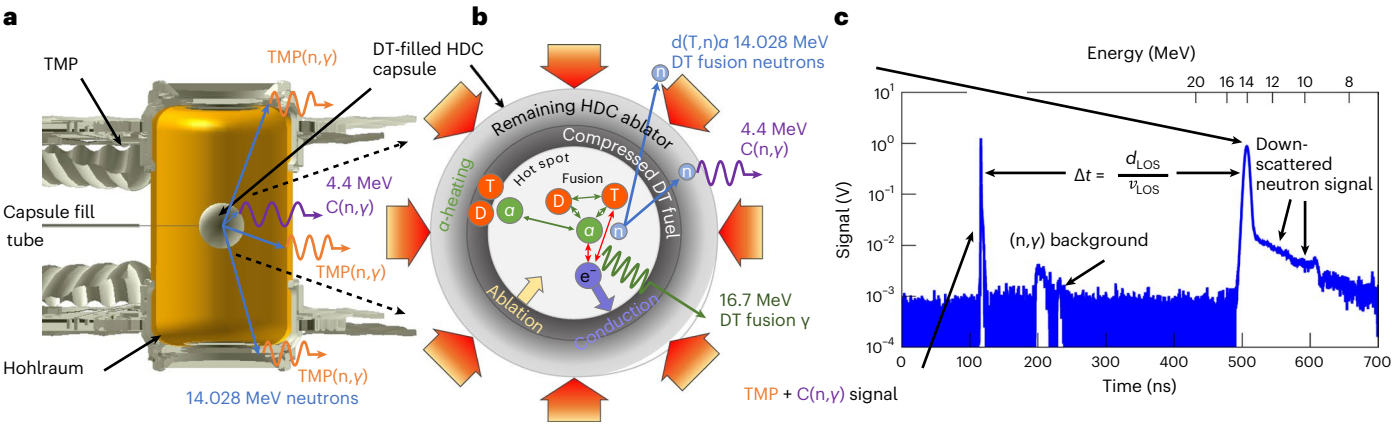

Fig. 1 | Indirect-drive inertial confinement fusion. a, Laser energy is converted into X-rays that compress and heat a spherical DT-filled capsule to generate fusion reactions. The HDC capsule is filled with DT gas through a fill tube and cryogenically frozen to create a solid DT ice layer on the inside surface. On heating and compression, the fusion of DT ions generates 14.028 MeV neutrons (blue) and γ-rays emitted by both fusion reaction and (n, γ) reactions in the surrounding capsule (purple) and the target TMP (orange). **b**, If heating of the compressed DT ice fuel by α-particles (green) emitted by the fusion reaction exceeds the radiation and electron conduction losses, the hot-spot reaction can become self-sustaining. **c**, The QCD nToF detectors on the NIF uniquely measure both γ- and neutron signals at approximately 100 and 500 ns, respectively. Low (n, γ) backgrounds enable a high-precision measurement of the mean line-of-sight neutron velocity v_{LOS} for a detector at distance d_{LOS}.

measurements, such as the implosion neutron yield (equivalent to the energy released), ion temperature, cold-fuel neutron opacity (down-scatter ratio) and capsule velocity, are obtained from five neutron spectrometers that view the implosion from different directions. Figure 1c provides an example of a neutron and γ-arrival time spectrum in a quartz Cherenkov detector (QCD).

Hydrodynamic models describing the implosions approximate the transport of α-particles through the burning plasma and cold fuel by diffusion, assuming that the mean free path of α-particles is short compared with the size of the burning region. In this approximation, the plasma is in local thermal equilibrium, where the ion velocity distribution is described by a Maxwellian with temperature T_{ion}, and a relationship exists between T_{ion} and the mean relative kinetic energy of the ions undergoing fusion, $\bar{K}$, can be described by[5–8]

$$\bar{K} = \frac{\int \mathrm{d}K\, K^2 \sigma(K) \mathrm{e}^{-K/T_{\mathrm{ion}}}}{\int \mathrm{d}K\, K \sigma(K) \mathrm{e}^{-K/T_{\mathrm{ion}}}}, \tag{1}$$

where $\sigma(K)$ is the fusion cross section and $\mathrm{e}^{-K/T_{\mathrm{ion}}}$ is the Maxwell–Boltzmann distribution. The general solution to equation (1) was described in other work[5,6,8] for different approximations, which we summarize here as

$$\bar{K} \to T_{\mathrm{ion}} \left[\left(\frac{T_{\mathrm{G}}}{T_{\mathrm{ion}}} \right)^{1/3} + \mathcal{F}(T_{\mathrm{ion}}) \right], \tag{2}$$

where $T_{\mathrm{G}} = 295.5$ keV for DT fusion and $\mathcal{F}(T_{\mathrm{ion}})$ is calculated using the DT fusion cross section (Methods).

Equation (2) has the physical interpretation that the ions with the highest likelihood of undergoing fusion occupy the tail of the Maxwell–Boltzmann distribution, for example, for $T_{\mathrm{ion}} = 4$ keV thermal plasma, $\bar{K} \approx 5T_{\mathrm{ion}}$ and is referred to as the 'Gamow' energy, first identified by Gamow[9]. At $T_{\mathrm{ion}} = 4$ keV, it is 5 e-foldings down from the distribution's maximum value.

The characteristics of the DT ion distribution are encoded by the neutrons generated by the fusion reactions in the plasma, enabling the determination of the plasma ion kinetic energy, ion temperature and plasma velocity moments from the neutron spectral moment. For the mean neutron energy,

$$\langle E_{\mathrm{n}} \rangle \approx 14.02839\ \mathrm{MeV} + 0.00056 \left[\langle u_{\parallel} \rangle + v_{\mathrm{iso}} \right], \tag{3}$$

where the velocities are in units of km s^{-1} and the 'isotropic velocity' is defined by

$$v_{\mathrm{iso}}(T_{\mathrm{ion}}) = 1.4641 \bar{K}(T_{\mathrm{ion}}) + 0.37969 T_{\mathrm{ion}}, \tag{4}$$

where $\bar{K}(T_{\mathrm{ion}})$ and T_{ion} are in units of keV, and the numeric coefficients are defined by the DT cross section and Maxwellian ion distribution. The ion temperature is typically determined from the second central moment or variance of the neutron spectrum as

$$\mathrm{Var}\,(E_{\mathrm{n}}) \approx 0.31401\,\mathrm{Var}\,(u_{\parallel}) + 6024.6 \langle T_{\mathrm{ion}} \rangle. \tag{5}$$

where again all terms are in units of keV. The symbol $\langle \cdot \rangle$ represents the burn average over the space and time moment of the plasma variables. Also, $u_{\parallel}$ is the projection of the plasma velocity along a particular direction (for example, the line of sight from the target to spectrometer). The isotropic velocity is the manifestation of the neutron energy upshift due to two physical factors: (1) additional relative velocity of the D and T ions in their centre-of-mass frame, leading to the first term in equation (4); (2) the motion of the the centre-of-mass frame that is related to the ion temperature and leads to the second term. A description of how the velocity and temperature is determined from the diagnostics is shown in Fig. 2.

Taking advantage of the relationship between the mean ion kinetic energy and ion temperature in a thermal plasma, a sufficiently precise determination of the isotropic velocity (equations (2) and (4)) would provide a measure of the ion temperature[10] independent from the plasma velocity variance in equation (5); we note that relativistically treating the neutron kinematics is essential in achieving this accuracy. The thermal or hydrodynamic expectation is then simply expressed as equation (4).

Equation (5) anticipates a source of neutron kinetic energy variance in addition to the average ion temperature. This term is due to the ion velocity variance as viewed along a line of sight that may result from flows generated inside the hot spot due to asymmetries in the implosion. The anisotropic component of this velocity variance appears as an anisotropic 'apparent T_{ion}' measured by the neutron diagnostics, denoted as T_{ion} in Table 1. The ion velocity variance could also contain radial components that would appear the same in all the directions and increase the apparent T_{ion} measurement. This was observed in another work[11] in which a comparison of the apparent T_{ion} values with

https://doi.org/10.1038/s41567-022-01809-3

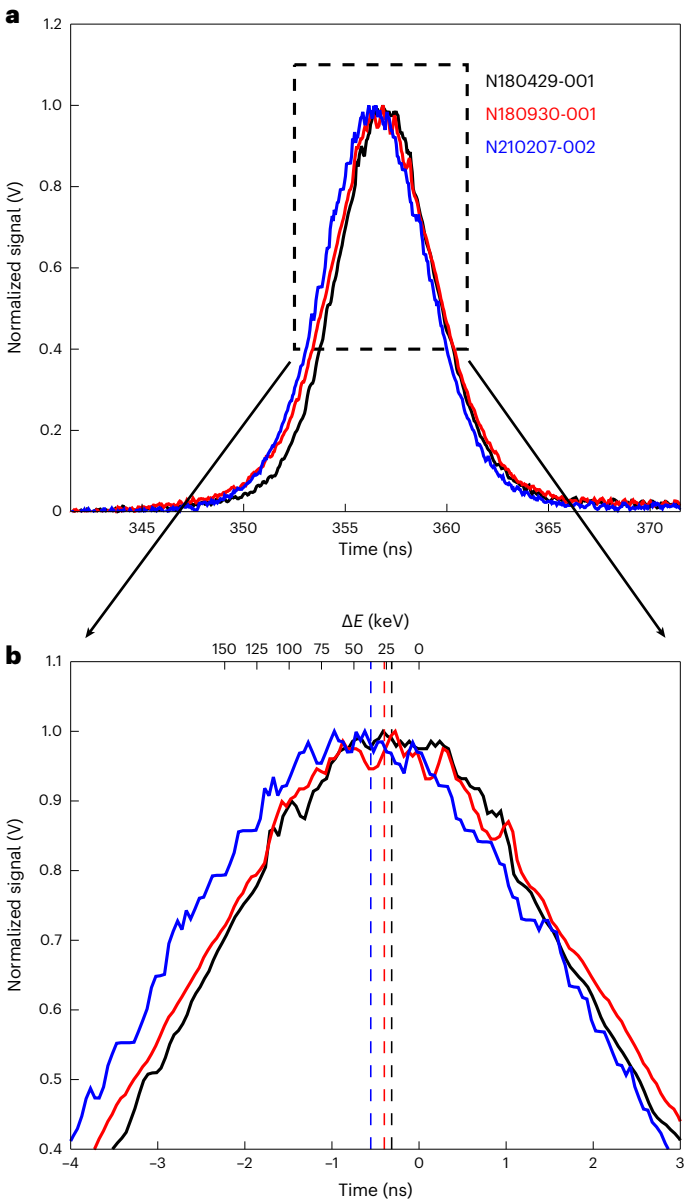

Fig. 2 | Neutron spectra recorded by a single line-of-sight QCD nToF detector. Normalized data for three shots are shown to compare the data from burning (N210207, blue) and non-burning (N180429, black; N180930, red) implosions. **a**, Raw data from the north-pole (NP) nToF are shown with the time axis corrected to the co-time of the γ-bang-time signals. **b**, By fitting all the five nToF lines of sight, the mode-1 component due to the bulk hot-spot velocity ($\vec{v}_{HS}$) can be determined and then removed for each individual line of sight ($\vec{v}_{HS} \cdot \hat{n}_{LOS}$) to reveal the different kinetic energy shifts ($\Delta E = 0.56037 v_{iso}$) and the different spectral widths (Var(E_n)). The mean neutron energy upshift ΔE is plotted on the top x axis for each shot and is shown as the dashed vertical line.

Table 1 | Neutron yield (Y_{DT}) and ion temperature (T_{ion}) data

	v_{iso}	Y_{DT}	T_{ion}	$v_{iso}(T)$	$T(v_{iso})$
Shot ID	**(km s^{-1})**	**(10^{16} neutrons)**	**(keV)**	**(km s^{-1})**	**(keV)**
N210207-002	59±2	5.29±0.16	5.67±0.14	42	9.03
N201122-002	56±3	3.21±0.10	5.17±0.13	39	8.31
N210605-001	54±3	4.11±0.13	5.86±0.12	43	7.86
N210220-001	54±3	4.99±0.13	5.54±0.14	41	7.86
N210307-004	54±2	4.40±0.14	5.53±0.12	41	7.86
N201101-001	54±3	3.04±0.08	4.95±0.12	38	7.86
N210328-001	51±2	1.93±0.05	5.43±0.14	41	7.21
N210117-002	45±3	1.40±0.05	4.26±0.12	34	6.01
N180930-001	41±2	1.53±0.04	5.50±0.12	41	5.34
N201011-001	40±3	0.84±0.03	4.38±0.12	35	5.09
N180429-001	38±2	0.83±0.03	4.61±0.14	36	4.67
N210418-003	36±2	1.06±0.03	4.33±0.12	34	4.40

Values for the implosions depicted with square symbols in Fig. 3 and the examples shown in Fig. 2 are shown in the first two columns. Here $v_{iso}(T)$ is the expected isotropic velocity[8] calculated from the nominal experimental value T_{ion}. The column labelled $T(v_{iso})$ lists the ion temperature for a Maxwell–Boltzmann plasma with the observed v_{iso}. The 1σ error bars for the measured v_{iso} and T_{ion} have not been propagated to their respective $T(v_{iso})$ and $v_{iso}(T)$ values.

the emissivity-weighted electron temperature shows that the neutron measurement overpredicts the electron temperature by hundreds of electronvolts.

The largest systematic uncertainty in the apparent T_{ion} measurement comes from uncertainties in the instrument response function[12]. Lacking an ion-temperature calibration source, the instrument response function is built from data (obtained in 'timing shots', intense and instantaneous pulses of γ-radiation, and exploding pushers for which the long-time tail of the signals is known to be free from the primary neutron scatter). The magnitude of this uncertainty is estimated to be 240 eV.

On each neutron yield shot, a suite of analysis codes are run to produce a set of scaler metrics for the shot. These scalers are then used to produce three-dimensional (3D) values, such as $\vec{v}_{HS}$, and scaler quantities averaged over multiple line-of-sight measurements such as v_{iso} and T_{ion}. Relationships like equation (1) can be used to assess the state of the plasma during the burn duration. Figure 3 shows the data for implosions using an HDC ablator with a cryogenic layer of solid DT and a central DT vapour. The laser pulse waveforms and the hohlraum dimensions change within this dataset.

Figure 3 shows that most of the low-yield implosions at the NIF (circles) are within systematic uncertainty to the expectation of a plasma described by a single-temperature Maxwellian. This region is shown below and right of the boundary indicated by equation (4) shown as the thick grey line in this figure. Here ten shots are highlighted with square symbols (more details in Table 1). This table lists the measured v_{iso} and T_{ion} values, and compares them, in the rightmost columns, with the two corresponding values calculated by equation (4). The first expectation in the column marked '$v_{iso}(T)$' in Table 1 assumes the measured T_{ion} value to calculate v_{iso}, whereas that in the column marked '$T(v_{iso})$' assumes the reverse and uses equation (4) to calculate the expected T_{ion} value using the measured v_{iso} value.

Two-dimensional (2D) simulations of similar implosions[13] are shown as a point cloud in Fig. 3 (the yield is colour coded) and using equations (5) and (4) for T_{ion} and v_{iso}, respectively, including all the higher moment terms. The simulation trends as it would for a single-temperature Maxwellian displaced by the plasma velocity distribution, which tends to increase T_{ion}. The increased T_{ion} value results in an increased yield along the ion kinetic energy boundary. The calculations represent a realistic instantiation of the hydrodynamics of these implosions and use particle Monte Carlo (PMC) simulations to transport the ions produced in the burn. The high-resolution 3D simulations[14] include more engineering features and drive asymmetries. These calculations simulate specific shots in the dataset shown in Fig. 3.

Confidence intervals are constructed using a Gaussian likelihood calculated from the region described by the simulation data. For each 'slice' of T_{ion}, a cumulative distribution function in v_{iso} of the summed Gaussian likelihoods provides the upper and lower limits for which the probability integrates to the confidence interval value. Out of the 44 measured data points, 11 are outside the 99% confidence interval

https://doi.org/10.1038/s41567-022-01809-3

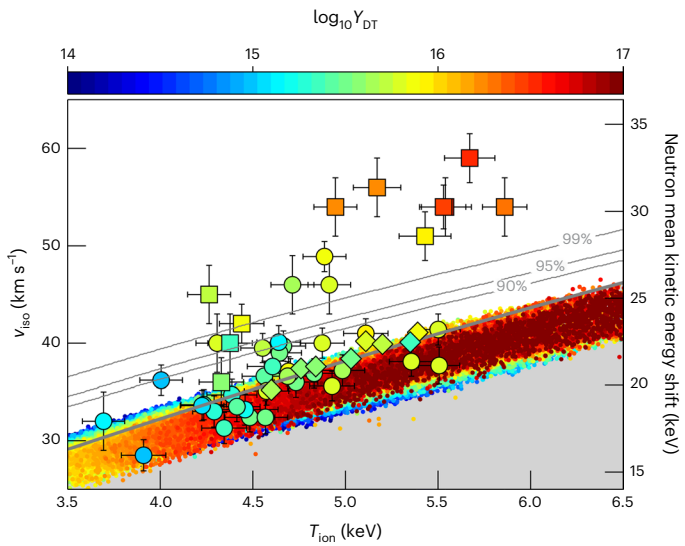

Fig. 3 | Interdependence of isotropic velocity (v_{iso}) and ion temperature (T_{ion}). Implosions of DT ignition capsules indicated by circles and squares symbols (the square symbols represent the data in Table 1) with uncertainties with the neutron yield (Y_{DT}) indicated as a colour code. The high-resolution 3D simulations are shown as diamonds. The boundary, namely, equation (4), is indicated by the thick black line. If a range of ion temperatures exist in the hot-spot plasma volume and during the time neutrons are generated, T_{ion} increases due to the increased velocity distribution, creating a 'hydrodynamically accessible' region (shaded grey) below the boundary. The 2D simulation ensemble for similar implosions is shown as the point cloud, using equations (5) for T_{ion} and equation (4) for v_{iso}, and colour coded for yield. This point cloud is bounded by the 90%, 95% and 99% confidence intervals, indicating the regions of expected statistical fluctuations of an implosion described by the simulation using $\delta v_{iso} = 3$ km s^{-1} and $\delta T_{ion} = 0.100$ keV. The mean neutron energy upshift equivalent to v_{iso} is plotted on the right axis. The error bars include contributions from systematic and 1σ statistical uncertainties.

and 8 belong to the HyE and I-Raum campaigns[15]. These implosions represent a departure from the behaviour expected by a plasma characterized by a single-ion-temperature Maxwellian ion distribution.

The neutron yield corrected for elastic scattering in the compressed DT fuel[16] (Y_{DT}) for these shots is plotted against the observed v_{iso} values (Fig. 4, square and circular data points) and compared with the equivalent data from 2D simulations (point could). Both are compared with the DT Maxwellian reactivity $\langle\overline{\sigma v}\rangle$ calculated using the T_{ion} value derived from the observed v_{iso} value. The solid line is scaled in the ordinate to best fit the data. To best match the simulations, the dashed line in Fig. 4 is not only scaled in the ordinate but also must be calculated using a T_{ion} value that is 2.5 times greater than that derived from v_{iso}. It is evident from this plot that the data is burning 'cooler' than the simulation for a given yield. The higher apparent T_{ion} value associated with the recent shots is consistent with an increase in the population of ion kinetic energy (≳10 keV). This ion population would be suprathermal; it does not exist as a consequence of the single-temperature Maxwellian that governs the behaviour of the majority of ions in the plasma for these implosions. The mean kinetic energy of the reacting ions is very sensitive to the shape of the ion kinetic energy distribution in this energy range as the DT fusion cross section is rapidly increasing. Small contributions of high-energy ions can increase the reactivity and shift $\langle\bar{K}\rangle$ to higher values; however, ions with energies much greater than the thermal energy also start to increase Var(E_n); therefore, these data place a unique constraint on the shape and energy of the DT ion distribution that is fusing and generating neutrons.

The upscattering of ions to higher energies through elastic collisions with the fusion α-particles can act to increase the higher-energy ion population; however, this is accounted for by PMC used in the simulations. The PMC samples a subset of ions and tracks them through the plasma until a specified kinetic energy of the scattered ion is reached—at which point the calculation stops and the remaining energy is deposited in that cell. Changing this parameter from 100 to 10 keV increases the yield by less than 10% in one-dimensional simulations and does not account for the increases in yield or v_{iso} observed in the data.

Other subtle changes to the neutron spectrum represented by skew and kurtosis as well as reaction-in-flight neutrons can also slightly move the mean neutron energy, but are estimated to contribute less than 1 km s^{-1} shifts in v_{iso}. The ion distributions described with multiple Maxwellians of different ion temperatures result in v_{iso} values below the boundary defined by equation (4).

We summarize the possible physical causes for the observed difference from Maxwellian into four general hypotheses: (1) kinetic, (2) hydrodynamic, (3) burn (temporal extent) and (4) burn (spatial extent).

For hypothesis (1), suprathermal DT ion distributions are predicted in some models that incorporate kinetic effects in the implosions[17,18]. However, most of the published studies on ion kinetic effects only consider the hot spot and start with higher ion temperatures than those existing in the implosions studied here[17–20]. The α-particles produced in DT fusion are suprathermal (having 3.5 MeV in a ~5 keV DT plasma), the majority of their kinetic energy comes from the Q value (17.59 MeV) of the fusion reaction, which is much larger than the ion temperature.

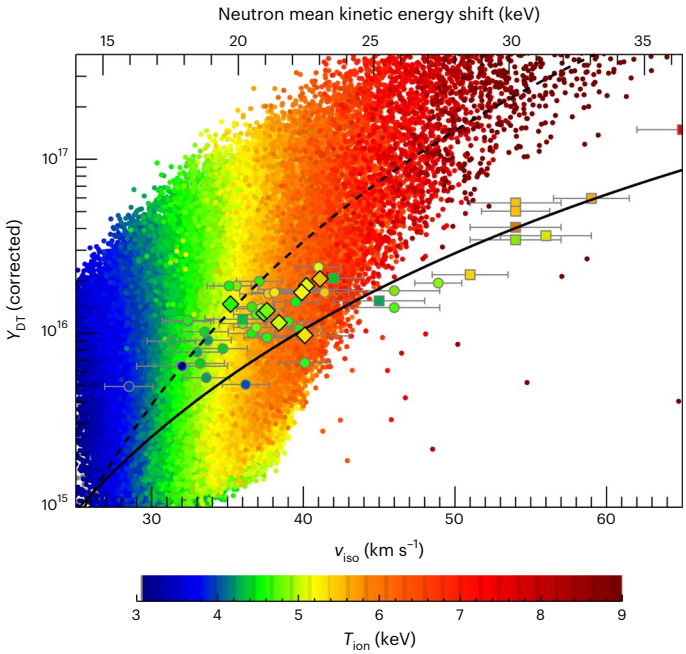

Fig. 4 | Relation between the measured neutron yield (Y_{DT}) and isotropic velocity (v_{iso}). This demonstrates that the data are burning at a cooler temperature than expected from the simulations. The top ordinate axis translates the measured v_{iso} value into the kinetic energy upshift (ΔE) that it represents in the centre-of-mass frame of the DT fusion reaction. Experimental data points are shown as circles and squares and the shots (listed in Table 1) are depicted as squares. The 2D simulation ensemble for similar implosions is shown as the point cloud, using equation (4) for v_{iso} and the calculated yield. High-resolution 3D simulations are shown as diamonds. The experimental neutron yield and 3D simulations are corrected to account for neutron scatter of the compressed fuel shell (Methods). The solid line is the Maxwellian reactivity $\langle\overline{\sigma v}\rangle$ calculated using T_{ion} derived from v_{iso} (equation (4)) and freely scaled to overlay the data. The dashed line is equivalent but using a 2.5 times higher ion temperature and freely scaled to overlay the data below the hydrodynamic boundary and 2D simulations. The error bars for neutron yield and v_{iso} include the systematic and 1σ statistical uncertainties.

https://doi.org/10.1038/s41567-022-01809-3

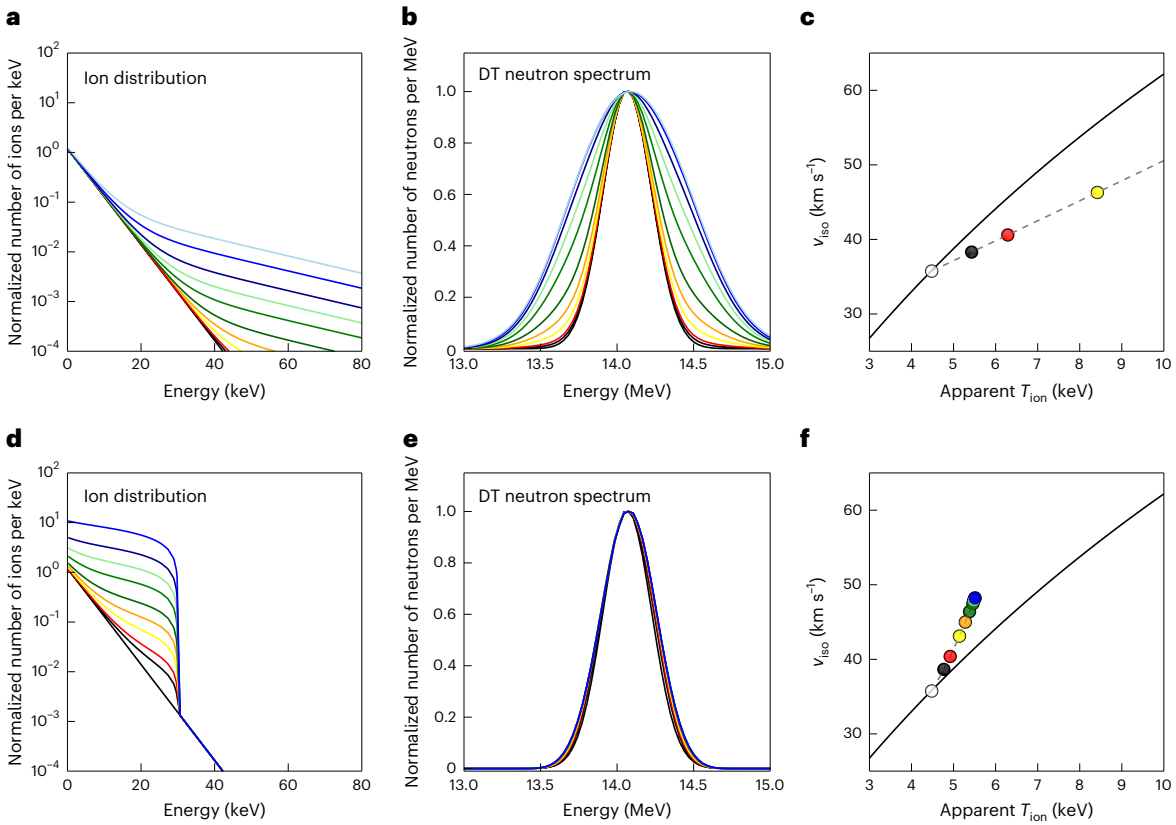

Fig. 5 | Neutron spectra generated by different DT ion distribution functions. **a**–**f**, Neutron spectra in **b** and **e** are derived from the ion distribution shown in **a** and **d**, respectively. **c** and **f** show the location of v_{iso} and T_{ion} calculated from the spectra in **b** and **e**, respectively, relative to the hydrodynamic boundary (Fig. 3, solid line). The distributions in **a** are two-temperature Maxwell–Boltzmann with increasing fractions (f_2) of the higher-temperature population. $T_1 = 4.5$ keV, $T_2 = 25.0$ keV and $f_2 = 0, 0.0004, 0.0008, 0.0020, 0.0040, 0.0080, 0.0200, 0.0400, 0.0800, 0.1600, 0.2800$. Distributions in **d** are described by a Maxwell–Boltzmann plus a tail with functional form $f_2\sqrt{E_{cut} - E}/\sqrt{E_{cut}}$ with an energy cut-off $E_{cut} = 35$ keV and increasing fractions (f_2). $T_1 = 4.5$ keV and $f_2 = 0, 0.07, 0.13, 0.27, 0.43, 0.60, 0.79, 0.88, 0.94, 0.97$. The colours represent increasing f_2 from grey, black, red, yellow, orange and green to blue. The dashed line represents the continuous locus for different fractions of the non-thermal population.

The details of how the α-particles transfer their energy to the surrounding plasma—plasmas that are at the temperatures and densities of the current NIF implosions (fuel-shell temperatures of ~1–2 keV and areal densities of ~1 g cm^{-2})—is an open experimental question. Hypothesis (2) results from the slight neutron opacity of the hot spot, which can lead to fewer neutrons from the far side of the hot spot (away from the spectrometer) reaching the detector than those emitted on the near side. This can act to upshift the mean neutron energy if the hot spot is radially expanding, but is present in the HYDRA simulations that should show this hydrodynamic behaviour. Hypothesis (3) requires a large (>10%) early time yield (for example, from the shock convergence in the capsule), shifting the mean of the total neutron time-of-flight (nToF) distribution early, generating an apparent isotropic velocity. Hypothesis (4) requires the neutron burn region separated from the presumed capsule centre of the order of 10 mm, and is ruled out by neutron images.

Two examples of how different suprathermal distributions (hypothesis (1)) can change the values of v_{iso} and T_{ion} are shown in Fig. 5, illustrating that to significantly move above the Maxwellian boundary requires a more 'boxy' distribution in which a suprathermal population exists with a cut-off in energy similar to that described in another work[17].

Experimental, theoretical and simulation work continues to identify the cause of this observation. The departure from Maxwellian plasma behaviour is a signature of this burning-plasma domain.

Online content

Any methods, additional references, Nature Research reporting summaries, source data, extended data, supplementary information, acknowledgements, peer review information; details of author contributions and competing interests; and statements of data and code availability are available at https://doi.org/10.1038/s41567-022-01809-3.

References

1. Lindl, J. Development of the indirect drive approach to inertial confinement fusion and the target physics basis for ignition and gain. *Phys. Plasmas* **2**, 3933–4024 (1995).
2. Christopherson, A. R. et al. Theory of alpha heating in inertial fusion: alpha-heating metrics and the onset of the burning-plasma regime. *Phys. Plasmas* **25**, 072704 (2018).
3. Zylstra, A. B. et al. Burning plasma achieved in inertial fusion. *Nature* **601**, 542–548 (2022).
4. Kritcher, A. L. et al. Design of inertial fusion implosions reaching the burning plasma regime. *Nat. Phys.* **18**, 251–258 (2022).
5. Brysk, H. Fusion neutron energies and spectra. *Plasma Phys.* **15**, 611–617 (1973).
6. Ballabio, L., Källane, J. & Gorini, G. Relativistic calculation of fusion product spectra for thermonuclear plasmas. *Nucl. Fusion* **38**, 1723–1735 (1998).
7. Appelbe, B. & Chittenden, J. Relativistically correct DD and DT neutron spectra. *High Energy Density Phys.* **11**, 30–35 (2014).

8. Munro, D. H. Interpreting inertial fusion neutron spectra. *Nucl. Fusion* **56**, 036001 (2016).
9. Gamow, G. Nuclear energy sources and stellar evolution. *Phys. Rev.* **53**, 595–604 (1938).
10. Moore, A. S. et al. The five line-of-sight neutron time-of-flight (nToF) suite on the National Ignition Facility (NIF). *Rev. Sci. Instrum.* **92**, 023516 (2021).
11. Jarrott, L. C. et al. Thermal temperature measurements of inertial fusion implosions. *Phys. Rev. Lett.* **121**, 085001 (2018).
12. Hatarik, R. et al. Analysis of the neutron time-of-flight spectra from inertial confinement fusion experiments. *J. Appl. Phys.* **118**, 184502 (2015).
13. Gaffney, J. A. et al. Making inertial confinement fusion models more predictive. *Phys. Plasmas* **26**, 082704 (2019).
14. Clark, D. S. et al. Three-dimensional modeling and hydrodynamic scaling of National Ignition Facility implosions. *Phys. Plasmas* **26**, 050601 (2019).
15. Ross, J. S. et al. Experiments conducted in the burning plasma regime with inertial fusion implosions. Preprint at https://arxiv.org/abs/2111.04640 (2021).
16. Rinderknecht, H. G. et al. Azimuthal drive asymmetry in inertial confinement fusion implosions on the National Ignition Facility. *Phys. Rev. Lett.* **124**, 145002 (2020).
17. Peigney, B. E., Larroche, O. & Tikhonchuk, V. Ion kinetic effects on the ignition and burn of inertial confinement fusion targets: a multi-scale approach. *Phys. Plasmas* **21**, 122709 (2014).
18. Sadler, J. D. et al. Kinetic simulations of fusion ignition with hot-spot ablator mix. *Phys. Rev. E* **100**, 033206 (2019).
19. Appelbe, B., Sherlock, M., El-Amiri, O., Walsh, C. & Chittenden, J. Modification of classical electron transport due to collisions between electrons and fast ions. *Phys. Plasmas* **26**, 102704 (2019).
20. Sherlock, M. & Rose, S. The persistence of Maxwellian D and T distributions during burn in inertial confinement fusion. *High Energy Density Phys.* **5**, 27–30 (2009).

Methods

Determining implosion attributes with nToF

Additions to nuclear diagnostics at the NIF, by the use of Cherenkov nToF spectrometers and by a fifth nToF line of sight[10], have improved the ability to detect implosion anisotropy through measurements of the neutron kinetic energy spectrum[21]. These high-precision measurements[22] simultaneously measure both γ-rays and neutrons emitted by nuclear reactions associated with only the fusion burn. Since the time-of-flight diagnostics integrate the neutron spectrum over the duration of the burn (of the order of 100–200 ps), distinguishing between neutrons emitted by the hot spot compared with those emitted by α-heating is not possible. However, the improved precision of the nToF measurements on NIF have uncovered distinguishing signatures of the neutron spectrum that are unique to the generation of a burning plasma.

The determination of the 'hot-spot velocity'—the average of the velocity of the DT ion pairs undergoing fusion—provides information on the capsule drive asymmetries[23] as well as the mean of the neutron kinetic energy distribution[10]. The ion temperature is determined by a forward fit of the nToF spectrum whose parameters include the variance in the neutron kinetic energy distribution[24], which includes not only the ion temperature but also the plasma velocity variance.

Multiple line-of-sight measurements of the neutron spectral moments are necessary to determine the hot spot and isotropic velocities. There are six nToF line-of-sight spectrometers with scintillator detectors capable of measuring the neutron kinetic energy spectrum[24–27]. Five of these lines of sight have an additional spectrometer system—the QCD[22] optimized to have high timing precision for high-yield implosions.

The QCD system measures the 'γ-flash', which is used to determine the time of flight of photons produced during the implosion. This is measured with a precision of ±25 ps. The γ-flash is created by a combination of processes (Fig. 1): the direct DT → ^{5}Heγ fusion channel, (n, γ) reactions on the carbon ablator that emit at 4.4 MeV and (n, γ) interactions with the thermal mechanical package (TMP), which is a part of the target system, and generates a broad spectrum of γ-rays up to about 8.0 MeV. The relatively low-energy Cherenkov threshold of the QCD system means that the signal is predominantly from the 1–5 MeV γ-rays emitted by the neutron reactions with the TMP and HDC ablator. Because of the finite flight time of the neutrons to these scattering sources, the γ-rays generated from these reactions arrive at the detector between 20 and 60 ps later than the fusion γ-rays. The QCD also measures the arrival time of the DT neutrons to ±16 ps, and the uncertainty of the 20 m flight path ($d_{\rm LOS}$) is ±1 mm. Figure 1c shows the raw data measured by the QCD nToF detectors demonstrates the high dynamic range of the γ- and neutron signals used to determine $v_{\rm LOS}$. The uncertainties in both γ- and neutron measurements combine to an overall line-of-sight velocity uncertainty of ±4.7 km s^{-1}.

The five line-of-sight measurements using the QCD spectrometers are fit to a four-parameter velocity model[21]: v_x, v_y, v_z and $v_{\rm iso}$, where the first three vector velocity components characterize the 'hot-spot velocity' associated with the mean velocity of burning-plasma in the lab frame and the fourth component is the 'isotropic' velocity. The mean neutron kinetic energy shift for a particular line of sight from equation (3) contains the following term:

$$\langle u_{\parallel}\rangle = v_{\rm LOS} \approx \vec{v}_{\rm HS}\cdot\hat{n}_{\rm LOS},$$

where $\hat{n}_{\rm LOS}$ is the direction vector of the line of sight.

This is illustrated in Fig. 2. The raw neutron spectra from one line of sight is shown in Fig. 2a and the time axis is corrected to account for the approximate 1 ns differences in implosion bang times for different experiments. Once the data from all the lines of sight are combined, the mode-1 component can be removed (Fig. 2b). This reveals the upshift in the mean neutron energy as $\Delta E = 0.56037 v_{\rm iso}$

Calculating $\mathcal{F}(T)$ from the DT fusion cross-section

The function $\mathcal{F}(T)$ is equal to 5/6 for the considerations elsewhere[5]. In the following discussion, we use the numerical results of Munro (table A.3 in ref. [8]) calculated using a relativistic expression for equation (1) and the ENDL2011 DT fusion cross-section evaluation, yielding

$$\mathcal{F}(T) = \frac{0.81857 + T(0.14272 + T(-0.0048217 + 1.1536\times10^{-5}T))}{1 + T(-0.0027543 + T(0.0092859 + 5.1419\times10^{-6}T))} \quad (6)$$

Equations (3)–(5) are from Munro's[8] equations (73) and (74) but include only the low-order terms. The coefficients are calculated using the data in ref. [8] and transformed to the coordinate system of the neutron kinetic energy, $E_{\rm n}$ (keV).

Neutron yield measurements

Neutron yields at the NIF are measured by the neutron activation of zirconium (Zr). Three Zr discs (radius, 34.9 mm; length, 7.5 mm) are positioned 4.559 m from the implosion. Neutrons emitted by the target travel to and interact with the ^{90}Zr atoms in the discs producing ^{89}Zr atoms via the $(n, 2n)$ reaction. The cross section of the $(n, 2n)$ reaction rises nearly linearly with the energy from a threshold of 12 MeV; therefore, the number of ^{89}Zr atoms produced is proportional to the number of DT neutrons. Noteworthily, ^{89}Zr is unstable and decays, emitting a 909 keV γ-ray with a half-life of 78.41 h. This half-life allows the pucks to be collected and transported to a counting facility in which the decays are energy analysed and counted for a fixed amount of time by a dedicated germanium detector. Accounting for the solid angle and collection efficiency of the detector, this measures the number of neutrons that leave the target to an uncertainty of $1\sigma \approx 5\%$. When 14.028 MeV 'primary' DT fusion neutrons generated in the hot spot leave the target, they must pass through compressed DT fuel (Fig. 1). The high areal density of the compressed fuel scatters the primary DT neutrons causing them to lose energy, and leading to a characteristic down-scattered tail to the neutron spectrum in addition to the primary DT fusion neutron peak. The amount of down-scatter is proportional to the compressed fuel areal density; in inertial confinement fusion experiments, it is typically characterized by the down-scatter ratio (DSR), which is the ratio of neutron yield between 10–12 MeV and 13–15 MeV. The compressed fuel density changes in different experiments; therefore, to calculate the fusion birth yield in the hot spot, the measured primary neutron yield must be corrected to account for the loss due to neutron scattering. This correction factor is approximately exp(3.8DSR(%)/100) derived from the average $(n, {\rm DT})$ scattering cross section (0.79*barns*) and the relation between areal density (ρ_r) and DSR. This correction has been applied to the primary neutron yield ($Y_{\rm n}$) values (Fig. 4)[16,28].

Impact of ion distributions on neutron spectra

The constraint of these measurements on the ion kinetic energy distribution can be assessed through the calculation of neutron spectra for somewhat arbitrarily chosen, non-Maxwellian ion distribution functions[29]. Two examples are shown in Fig. 5. In Fig. 5a–c, a simple two-temperature Maxwell–Boltzmann ion distribution is used and the moments of the resulting neutron spectrum are plotted in Fig. 5b and $v_{\rm iso}$ and $T_{\rm ion}$ calculated from the spectrum are shown in Fig. 5c relative to the thermal expectation (or boundary) described by equation (4). An equivalent analysis is performed for an arbitrarily chosen ion distribution function that adds a tail to a Maxwell–Boltzmann distribution in Fig. 5d–f. The tail is described by $f_2\sqrt{E_{\rm cut}-E}/\sqrt{E_{\rm cut}}$. These two figures illustrate how ion distributions with a high energy population tend to increase the variance of the neutron spectrum (from which $T_{\rm ion}$ is derived) more quickly than the mean neutron energy associated with $v_{\rm iso}$. The alternative is true when a suprathermal population is limited to energies below a certain cut-off energy and the $v_{\rm iso}$ point lies above the thermal expectation boundary. It is worth noting that this is

reminiscent of the kinetic α-particle energy deposition model described in another work[17] in which 3.5 MeV α-particles gradually lose energy to electrons until they reach a critical velocity at which they couple more strongly to the ion population.

Data availability

Raw data were generated at the National Ignition Facility and are not available to the general public. Derived experimental data supporting the findings of this study shown in Figs. 3 and 4, but not in Table 1 are available from the corresponding authors upon reasonable request.

Code availability

The simulation codes used in this manuscript are not available to the general public.

References

21. Hartouni, E. P. et al. Optimal choice of multiple line-of-sight measurements determining plasma hotspot velocity at the National Ignition Facility. *Rev. Sci. Instrum.* **92**, 023513 (2021).
22. Moore, A. S. et al. A fused silica Cherenkov radiator for high precision time-of-flight measurement of DT γ and neutron spectra (invited). *Rev. Sci. Instrum.* **89**, 101120 (2018).
23. Spears, B. K. et al. Mode 1 drive asymmetry in inertial confinement fusion implosions on the National Ignition Facility. *Phys. Plasmas* **21**, 042702 (2014).
24. Hatarik, R. et al. A new neutron time-of-flight detector to measure the MeV neutron spectrum at the National Ignition Facility. *Plasma Fusion Res.* **9**, 4404104 (2014).
25. Grim, G. P. et al. The 27.3 meter neutron time-of-flight system for the National Ignition Facility. In *Penetrating Radiation Systems and Applications XIV* (eds. Grim, G. P. & Barber, H. B.) **8854**, 70–81 (SPIE, 2013).
26. Clancy, T. J. et al. Engineering architecture of the neutron time-of-flight (nToF) diagnostic suite at the National Ignition Facility. In *Target Diagnostics Physics and Engineering for Inertial Confinement Fusion III* (eds. Bell, P. M. & Grim, G. P.) **9211**, 92110A (SPIE, 2014).
27. Caggiano, J. A. et al. Design of a north pole neutron time-of-flight (NTOF) system at NIF. *J. Phys.: Conf. Ser.* **717**, 012087 (2016).
28. Meaney, K. D. et al. Total fusion yield measurements using deuterium–tritium gamma rays. *Phys. Plasmas* **28**, 102702 (2021).
29. Crilly, A. et al. Constraints on ion velocity distributions from fusion product spectroscopy. *Nucl. Fusion* **62**, 126015 (2022).

Acknowledgements

We would like to acknowledge many discussions with our colleagues O. Landen, P. Patel, L. Divol, P. Springer and C. Cerjan. Lawrence Livermore National Laboratory is operated by Lawrence Livermore National Security for the US Department of Energy, National Nuclear Security Administration, under contract no. DE-AC52- 07NA27344. This Article (LLNL-JRNL-824268) was prepared as an account of work sponsored by an agency of the US government. Neither the US government nor Lawrence Livermore National Security, nor any of their employees make any warranty, expressed or implied, or assume any legal liability or responsibility for the accuracy, completeness, or usefulness of any information, apparatus, product, or process disclosed, or represent that its use would not infringe privately owned rights. The views and opinions of authors expressed herein do not necessarily state or reflect those of the US government or Lawrence Livermore National Security and shall not be used for advertising or product endorsement purposes.

Author contributions

E.P.H.: neutron diagnostics, wrote sections of paper. A.S.M.: neutron diagnostics, wrote sections of paper. A.J.C.: theory. B.D.A. theory. P.A.A.: hohlraum physics. K.L.B.: hybrid 'shot RI' (shot responsible individual). D.T.C.: hybrid shot RI. D.S.C.: high-resolution 3D simulations. T.D.: hybrid shot RI. M.J.E.: nToF diagnostics. J.E.F.: simulation methods. M.G.J.: neutron diagnostics. G.P.G.: neutron diagnostics development. R.H.: neutron diagnostics development and analysis code. J.J.: neutron diagnostics deployment and operations. S.M.K.: neutron diagnostics deployment and operations. J.K.: neutron diagnostics development. A.L.K.: hybrid-E design lead. K.D.M.: γ-ray diagnostics. J.L.M.: high-resolution 3D simulations. D.H.M.: theory methodology. R.C.N.: post-shot simulations. A.E.P.: hybrid and I-Raum shot RI. J.E.R.: N201101 and N210207 experimentalist and shot RI. H.F.R.: original I-Raum design lead. J.S.R.: I-Raum experimental lead and N201122 shot RI. D.J.S.: neutron diagnostics. S.M.S.: HYDRA details. B.K.S.: simulations lead. C.V.Y.: present I-Raum design lead. A.B.Z.: hybrid-E experimental lead.

Competing interests

The authors declare no competing interests.

Additional information

Correspondence and requests for materials should be addressed to E. P. Hartouni, A. S. Moore or A. J. Crilly.

Peer review information *Nature Physics* thanks Alessio Morace, Peter Norreys and the other, anonymous, reviewer(s) for their contribution to the peer review of this work.

Reprints and permissions information is available at www.nature.com/reprints.